

Interferometric Confirmation of Radiation-Pressure Effects in Laser-Plasma Interactions

D. T. Attwood, D. W. Sweeney,^(a) J. M. Auerbach, and P. H. Y. Lee

Lawrence Livermore Laboratory, University of California, Livermore, California 94550

(Received 17 October 1977)

Interferometric data resolved to $1\ \mu\text{m}$ and 15 psec confirm the significant role of radiation pressure during high-intensity laser-plasma interactions. Specifically observed manifestations include electron density profiles steepened to $\sim 1\text{-}\mu\text{m}$ scale length, clearly defined upper and lower density shelves, and small- and large-scale deformations of transverse isodensity of surfaces.

Prompted by current interest in laser-induced fusion, a number of papers have recently been published concerning the interaction of intense laser light with the plasma surrounding irradiated targets, and in particular the significant role of radiation pressure in both large- and small-scale deformations of the critical surface. The literature describes optical absorption and scattering in the presence of self-steepened electron density profiles,¹ density cavities, and generalized modulation of the critical surface.² Reports to date have been limited primarily to theoretical and computational studies because of the stringent experimental requirements, viz., space-time resolution of microns and picoseconds are essential for measurements during irradiation. Supporting experimental work of an indirect nature,³ and on larger space-time scales has appeared.⁴ The collective thrust of these papers is that radiation pressure modifies and deforms the critical surface when the energy density of the incident radiation is comparable to the thermal energy density of the plasma, and that these modifications in turn affect the absorption and transport of energy. In particular, it is predicted that these effects enhance the role of resonance absorption while reducing that due to parametric and collisional processes, which require shallow axial gradients.⁵ The existence of profile steepening to supercritical values is particularly significant for long-wavelength laser interactions because it places high-density plasma in close proximity to the absorption region. With more carriers available, transport of energy to the core is enhanced and excessive corona heating is minimized. In this Letter we present the first interferometric data with sufficient space-time resolution, $1\ \mu\text{m}$ and 15 psec, to directly confirm the presence of profile steepening, hole formation, and transverse rippling of the critical surface during irradiation by high-intensity Nd-laser pulses.

The interaction experiments were performed at $1.06\text{-}\mu\text{m}$ wavelength with one beam of Livermore's Janus laser facility,⁶ operating in this case with nominally 0.5–5-J, 30-psec full width at half-maximum pulses, and $f/10$ focusing optics. Laser prepulse was measured with a threshold of $10\ \mu\text{J}$. Targets consisted of $40\text{-}\mu\text{m}$ -diam SiO_2 glass microballoons, and $50\text{--}300\text{-}\mu\text{m}$ -diam glass and Parylene disks. Electron temperatures, as deduced from a space-time integrated x-ray K -edge filter technique,⁷ ranged from 0.7 to 1 keV in these experiments.

Electron densities were measured interferometrically with a double-exposure holographic technique⁸ employing corrected $f/2.5$ optics and a $2660\text{-}\text{\AA}$ probe pulse of several microjoules energy and 15 psec duration. The probe pulse was split from the main laser pulse just after the oscillator switchout, and then separately amplified, filtered, and shaped. Uniform backlighting of targets was accomplished by maintaining the B integral⁹ below a value of 0.5. Frequency conversion was accomplished in successive potassium dihydrogen phosphate and ammonium dihydrogen phosphate frequency-doubling crystals. Conversion efficiency was set at a modest level to maximize pulse shortening.⁹ Small target diameters were chosen to minimize the deleterious effects of probe-beam refraction during passage through the strong axial gradient density field.⁸ The probe pulse was synchronized with the $1.06\text{-}\mu\text{m}$ heating pulse to an accuracy of approximately 10 psec by streak photography.

A sample interferogram, obtained within 10 psec of peak intensity, is shown in Fig. 1(a) for a $41\text{-}\mu\text{m}$ -diam, $0.6\text{-}\mu\text{m}$ -thick spherical glass microshell. Peak intensity for this experiment was approximately $3 \times 10^{14}\ \text{W}/\text{cm}^2$. A silhouette of the original ball is overlaid for reference. Abel-inverted electron densities¹⁰ are shown in Fig. 1(b) for a transverse plane $4\ \mu\text{m}$ from the original target surface. The $21\text{-}\mu\text{m}$ transverse

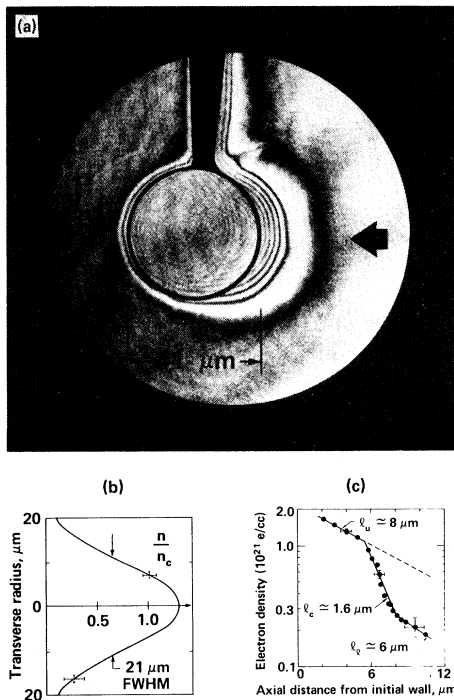


FIG. 1. (a) Interferogram at peak irradiation of a 41- μm -diam ball. $I \approx 3 \times 10^{14} \text{ W/cm}^2$. (b) Transverse electron density profile at an axial position 4 μm from the initial target wall. (c) Density profile on axis, demonstrating steepening due to radiation pressure. Solid lines are best fit; e -folding scale lengths l_u , l_c , and l_l are indicated for the upper, critical, and lower density regions. Typical error bars are shown in (b) and (c); $n_c = 10^{21} \text{ e/cm}^3$.

scale is significant in that probing to critical electron density (10^{21} e/cm^3), in this strongly refractive medium, is only possible along a short probing path. Densities along the symmetry (irradiation) axis are shown in Fig. 1(c), along with typical error bars. Each point is obtained from the axial value of a transverse plot similar to Fig. 1(b). A three-line best fit is included in Fig. 1(c) for comparison with theory which, to lowest order, is simply a balance at the critical surface of thermal pressure on the high side with thermal and uniform radiation pressure on the subcritical side. The most important feature of this simple model, which is sustained by the inclusion of detailed plasma and hydrodynamic processes,¹ is that clearly defined subcritical and supercritical density shelves exist with a separation of less than 1 μm . The intersection of the lines in Fig. 1(c) permits us to identify the upper and lower density shelves in that experiment, and separately determine scale lengths

in these regions. The measured critical-region scale length of 1.6 μm is undoubtedly larger than predicted values because of the finite 1- μm spatial resolution, and departures from cylindrical symmetry.

For the experiment of Fig. 1 we estimate the ratio of radiation to thermal pressure to be $P_r/P_{th} \approx 1.7I_0/cn_kT \approx 0.2$ (see Estabrook *et al.*, Ref. 1, for a lower shelf density of $0.3n_c$, near normal incidence, and a roundtrip fractional absorption of 30%). Using an isothermal model of mass and momentum balance at a sonic critical surface, Kidder has shown¹¹ that a density step $\Delta n/n_c \approx (P_r/P_{th})^{1/2} \approx 0.4$ is to be expected for the experiment of Fig. 1. More recent calculations and simulations by Lee *et al.*¹ predict a similar result, except that the more detailed treatment predicts both upper and lower density shelf values, not just the difference. In this case, $V_0/V_{th} \approx 0.3$, they predict values of $1.2n_c$ and $0.6n_c$, whereas Fig. 1(c) suggests experimental values of $1.1n_c$ and $0.3n_c$. The upper-shelf values are within the experimental uncertainty. In addition, the 2D (two-dimensional) experimental geometry permits significant transverse flow of plasma, which tends to reduce the pressure on axis and thus produce a supercritical density value less than predicted by a 1D theory. Comparison in the lower-shelf region is less favorable, perhaps because of larger error bars, but possibly because of unresolved temperature differences in the subcritical and supercritical regions. As pointed out by Estabrook, Valeo, and Kruer^{1,11} subcritical plasma heating, localized by micron-sized skin depth and electron mean free paths, may lead or add to density step size in experiments such as reported here.

Further evidence supporting the role of radiation pressure is observed in our flat-disk experiments. At high intensity these flat targets display a large-scale density hole with transverse scale size qualitatively similar to that of the incident light. Sample interferograms at 3×10^{13} and $3 \times 10^{14} \text{ W/cm}^2$ are presented in Fig. 2. General features of the fringe patterns permit one to make several interesting observations without recourse to numerical inversion. For instance, the fact that inner fringes run parallel to the original target surface in Fig. 2(b), rather than bowing out, is clear evidence of a large-scale density hole on axis. Hole formation is observed in all our disk experiments at intensities $\geq 3 \times 10^{14} \text{ W/cm}^2$, including both low- and high- Z materials. The effect is not observed at low intensity, as in

Fig. 2(a), where bowed fringes are observed. Numerically inverted profiles, seen in Figs. 2(c) and 2(d), quantify hole formation and provide more graphic evidence of nonuniform radiation pressure pushing plasma from the high-intensity region.

Figure 3 shows the strongly rippled fringe pattern typical of our $I \geq 10^{15}$ W/cm² Parylene-disk experiments. Because of the strong correlation between localized fringe and density fluctuations, one can readily infer typical electron-density variations of 20% amplitude and 10- μ m scale length directly from Fig. 3, without recourse to numerical inversion. These results suggest that an accurate model of resonance absorption should include both large-scale hole formation and small-scale surface rippling.¹² It is worth noting that rippling was not observed in any of our ball experiments.

In conclusion, we have presented well-resolved electron density distributions which show clearly and directly the role of radiation pressure in plasmas produced by intense laser light. In sample results we see gradient steepening, quantitatively determined density jumps, hole formation, and small-scale rippling of the isodensity surfaces.

The authors acknowledge the excellent technical assistance of E. L. Pierce, and the encour-

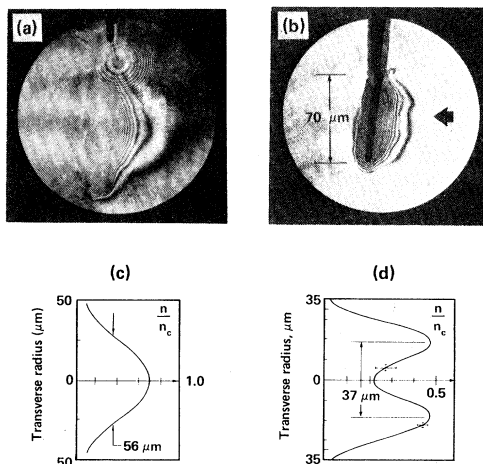


FIG. 2. (a) Interferogram of a 170- μ m-diam, 8- μ m-thick Parylene disk, 10 psec after peak intensity. $I \approx 3 \times 10^{13}$ W/cm². (b) Same for a 70- μ m diam, 1- μ m thick tungsten glass disk. $I \approx 3 \times 10^{14}$ W/cm². (c) Transverse electron-density profile, inverted about the irradiation symmetry axis, shows no cavity for low-intensity experiment. (d) Similar transverse profile, 16 μ m from initial surface, showing the hole formed by radiation pressure in a high-intensity experiment.

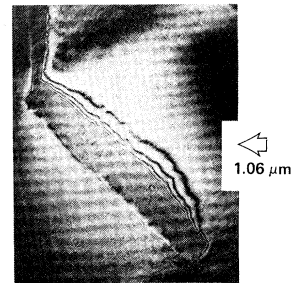


FIG. 3. Interferogram of a 350- μ m diam, 22- μ m-thick Parylene disk irradiated at 48° incidence angle with *p*-polarized light. $I \approx 3 \times 10^{15}$ W/cm². Strongly rippled, unbowed fringes indicate that both large-scale hole formation and small-scale rippling play significant roles in the absorption process.

agement and material support of their many colleagues in the Livermore Laser Fusion program, particularly C. E. Max, C. W. Hatcher, W. L. Kruer, J. E. Swain, L. W. Coleman, H. G. Ahlstrom, and C. D. Hendricks. This work was performed under the auspices of the U. S. Department of Energy.

(a) Permanent address: Purdue University, West Lafayette, Ind. 47907.

¹K. G. Estabrook, E. J. Valeo, and W. L. Kruer, *Phys. Fluids* **18**, 1151 (1975); K. Lee, D. W. Forslund, J. M. Kindel, and E. L. Lindman, *Phys. Fluids* **20**, 51 (1977); J. A. Stamper, *Phys. Fluids* **18**, 735 (1975).

²E. J. Valeo and K. G. Estabrook, *Phys. Rev. Lett.* **34**, 1008 (1975); K. G. Estabrook, *Phys. Fluids* **20**, 51 (1977).

³S. Jackel, B. Perry, and M. Lubin, *Phys. Rev. Lett.* **37**, 95 (1976); D. M. Phillion, R. A. Lerche, V. C. Rupert, R. A. Haas, and M. J. Boyle, *Phys. Fluids* **20**, 1892 (1977).

⁴T. P. Donaldson and I. J. Spalding, *Phys. Rev. Lett.* **36**, 467 (1976); R. Fedosejevs, I. V. Tomov, N. H. Burnett, G. D. Enright, and M. C. Richardson, *Phys. Rev. Lett.* **39**, 932 (1977); H. Azechi, S. Oda, K. Tanaka, T. Norimatsu, T. Sasaki, T. Yamanaka, and C. Yamanaka, *Phys. Rev. Lett.* **39**, 1144 (1977).

⁵F. W. Perkins and J. Flick, *Phys. Fluids* **14**, 2012 (1971); C. S. Liu, M. N. Rosenbluth, and R. B. White, *Phys. Fluids* **17**, 1211 (1974).

⁶J. F. Holzrichter and D. R. Speck, *J. Appl. Phys.* **47**, 2459 (1976).

⁷V. W. Slivinsky, H. N. Kornblum, and H. D. Shay, *J. Appl. Phys.* **46**, 1973 (1975).

⁸D. T. Attwood, L. W. Coleman, and D. W. Sweeney, *Appl. Phys. Lett.* **26**, 616 (1975); D. T. Attwood, in *Proceedings of the Twelfth International Congress on High Speed Photography*, Toronto, August 1976, edited by M. C. Richardson (to be published); the primary advantages of this technique, in addition to providing the desired 1- μ m resolution, are that it provides simple and

accurate focusing, a necessary feature for strongly refracting media, and that it is relatively unaffected by harmonic emission from the plasma.

⁹D. T. Attwood, E. S. Bliss, E. L. Pierce, and L. W. Coleman, *IEEE J. Quant. Elec.* **12**, 203 (1976); D. T. Attwood, E. L. Pierce, and L. W. Coleman, *Opt. Commun.* **15**, 10 (1975).

¹⁰D. W. Sweeney, D. T. Attwood, and L. W. Coleman,

Appl. Opt. **15**, 1126 (1976).

¹¹R. E. Kidder, Lawrence Livermore Laboratory Report No. UCRL-74040, 1972 (unpublished); K. J. Estabrook, E. Valeo, and W. L. Kruer, *Phys. Lett.* **49A**, 109 (1974).

¹²K. R. Manes, V. C. Rupert, J. M. Auerbach, P. H. Y. Lee, and J. E. Swain, *Phys. Rev. Lett.* **39**, 281 (1977).

Theoretical Analysis of Bound-State Resonance Data in He-LiF Scattering

Charles E. Harvie and John H. Weare

Department of Chemistry, Revelle College, University of California—San Diego, La Jolla, California 92093

(Received 28 October 1977)

The He-LiF selective-adsorption data of Frankl and co-workers are analyzed using an attractive-well, corrugated-wall model. The model is solved to convergence by an expansion method. The calculated He-LiF spectrum is in good agreement with experiment. Calculations show that the intensity of weakly bound states is enhanced by band splitting with stronger resonances. This may provide a method for observing these states.

Recently there has been a great deal of experimental and theoretical interest in the scattering of He beams from solid surfaces. For systems such as LiF at low surface temperatures, the scattering features are predominantly elastic (diffractive). At sufficiently low beam energies or large incident angles the elastic intensity is dominated by contributions from combined state resonances in the attractive surface-averaged potential $V_{00}(z)$. These resonances are commonly known as selective adsorptions. As is well known they lead to a rather detailed knowledge of the bound states of $V_{00}(z)$.

In this article, we discuss the selective adsorption data of Frankl and co-workers¹ by introducing an attractive-well, corrugated-wall model of atom-surface scattering. The solution to the model utilizes a Rayleigh expansion.² The resulting matrix equation is solved as a series expansion. The theory is applied to the He-LiF system, and is shown to be in good agreement with experiment. The method provides an inexpensive means to parametrize surface potentials and explain complex regions in the experimental data.

As has become apparent from a wide range of investigations,³ the atom-surface potential may be characterized by a short-ranged strongly repulsive region and a long-ranged weakly attractive region. With these features in mind we use a model potential defined as

$$V(X, z) = \begin{cases} \infty, & z > \epsilon\sigma(X), \\ V_a(z), & z < \epsilon\sigma(X). \end{cases} \quad (1)$$

z is normal to the surface and $X = (x, y)$. $V_a(z)$ is general and is used to fit the experimental data. Square-well attractive potentials with the corrugated wall have been investigated by other authors.⁴ $\sigma(X)$ is a periodic function with the periodicity of the surface. ϵ is the coupling parameter representing the strength of periodicity of the surface. For the purposes of this Letter $\sigma(X)$ will be taken as $\cos(2\pi x/\alpha) + \cos(2\pi y/\alpha)$, although higher Fourier terms may be included with little difficulty. The parameter α is the lattice spacing on the surface.

By use of the Rayleigh hypothesis the total wave function is expanded in the series

$$\psi_{k_0, K}(X, z) = \varphi_{k_0}^{(-)} e^{iK \cdot X} - \sum_G B_G \varphi_{k_G}^{(+)} e^{i(K+G) \cdot X}. \quad (2)$$

K is the parallel translational wave vector (k_x, k_y) , and G is a reciprocal lattice vector $(2\pi n/\alpha, 2\pi m/\alpha)$. k_G , the perpendicular wave vector for channel G , is given by the usual conservation of energy relation. The functions $\varphi_{k_G}^{(\pm)}(z)$ are the solutions to the one-dimensional Schrödinger equation for $V_a(z)$, having $\exp(\pm ik_G z)$ asymptotic behavior for open channels and $\exp(\mp |k_G| z)$ behavior for closed channels. The transition probability to a given open diffractive channel G is proportional to $|B_G|^2$. The wave function in Eq. (2) must vanish at the infinite barrier [when $z = \epsilon\sigma(X)$ in Eq. (1)]. This boundary condition gives the following matrix equation for the scattering amplitudes, B_G :

$$\sum_{G'} A_{G, G'}^{(+)}(\epsilon) B_{G'}(\epsilon) = A_{G, 0}^{(-)}(\epsilon), \quad (3)$$

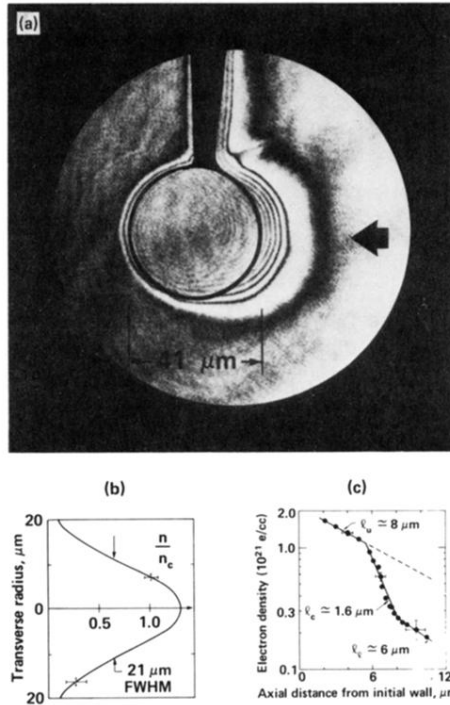


FIG. 1. (a) Interferogram at peak irradiation of a 41- μm -diam ball. $I \approx 3 \times 10^{14} \text{ W/cm}^2$. (b) Transverse electron density profile at an axial position 4 μm from the initial target wall. (c) Density profile on axis, demonstrating steepening due to radiation pressure. Solid lines are best fit; e -folding scale lengths l_u , l_c , and l_l are indicated for the upper, critical, and lower density regions. Typical error bars are shown in (b) and (c); $n_c = 10^{21} \text{ e/cm}^3$.

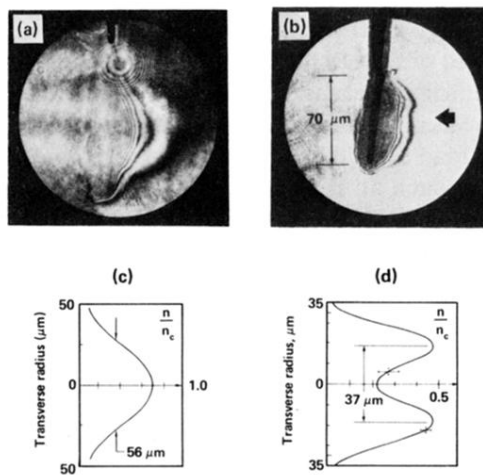


FIG. 2. (a) Interferogram of a 170- μm -diam, 8- μm -thick Parylene disk, 10 psec after peak intensity. $I \approx 3 \times 10^{13} \text{ W/cm}^2$. (b) Same for a 70- μm diam, 1- μm thick tungsten glass disk. $I \approx 3 \times 10^{14} \text{ W/cm}^2$. (c) Transverse electron-density profile, inverted about the irradiation symmetry axis, shows no cavity for low-intensity experiment. (d) Similar transverse profile, 16 μm from initial surface, showing the hole formed by radiation pressure in a high-intensity experiment.

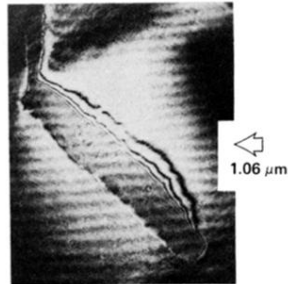


FIG. 3. Interferogram of a 350- μm diam, 22- μm -thick Parylene disk irradiated at 48° incidence angle with p -polarized light. $I \approx 3 \times 10^{15}$ W/cm². Strongly rippled, unbowed fringes indicate that both large-scale hole formation and small-scale rippling play significant roles in the absorption process.